Extending the Spectral Integral Method to Solving 3-D Electromagnetic Scattering From a Smooth Sphere

Zhen Guan, Jiawen Li, Falin Liu, and Feng Han, *Senior Member, IEEE*

***Abstract*—Previous works have shown that due to its high-order accuracy with exponential convergence, the spectral integral method (SIM) significantly outperforms the traditional surface integral equation (SIE) for computing electromagnetic (EM) scattering from 2-D homogeneous objects with smooth boundaries (e.g., infinitely long circular cylinders) in terms of memory and time cost. This work extends SIM to the computation of EM scattering from smooth 3-D spheres filled with metal or homogeneous dielectric materials. Starting from the traditional SIE, the unknown spatial-domain equivalent electric and magnetic currents on the sphere surface are expanded by truncated vector spherical harmonics (VSH) series with unknown coefficients. Then the dyadic Green's functions (DGFs) directly interact with VSH and thus are transformed into their spherical-harmonic spectral coefficients by surface integrals. Consequently, the conventional spatial-domain convolutional integrals in the SIE are transformed into multiplications of VSH spectral coefficients. Finally, to maintain the reliability of the SIM solution, the discretized equations are constructed by sampling the field values at the perturbed spherical Fibonacci grids (SFGs). To justify the computation accuracy and implementation efficiency of SIM applied to EM scattering from metal and dielectric spheres, a few numerical experiments were conducted, comparing it to the traditional SIE method. It is found that SIM only needs the spatial sampling density (SD) of 4 points per wavelength (PPW) to achieve reliable computation results while the traditional SIE usually requires an SD of 25 PPW to reach the same accuracy. In addition, the dependence of the required number of VSH modes to accurately represent the scattered fields on the distance between the excitation source and the scatterer is also studied.**

***Index Terms*—Dielectric sphere, electromagnetic (EM) scattering, metal sphere, spectral integral method (SIM), surface integral equation (SIE).**

Received 7 January 2026; accepted 7 February 2026. This work was supported by the National Natural Science Foundation of China under Grant 62271428. *(Corresponding author: Feng Han.)*

Zhen Guan is with the Great Bay Institute for Advanced Study, Dongguan 523000, China, also with the School of Computing and Information Technology, Great Bay University, Dongguan 523000, China, and also with the School of Information Science and Technology, University of Science and Technology of China, Hefei 230027, China (e-mail: zguan@gbu.edu.cn).

Jiawen Li is with Guangxi Key Laboratory of Brain-Inspired Computing and Intelligent Chips, School of Electronic and Information Engineering, and the Key Laboratory of Integrated Circuits and Microsystems, Education Department of Guangxi Zhuang Autonomous Region, Guangxi Normal University, Guilin 541004, China (e-mail: jiawenli@mailbox.gxnu.edu.cn).

Falin Liu is with the Department of Electronic Engineering and Information Science, University of Science and Technology of China, Hefei 230027, China (e-mail: liufl@ustc.edu.cn).

Feng Han is with the School of Computing and Information Technology, Great Bay University, Dongguan 523000, China, and also with the Institute of Electromagnetics and Acoustics, Xiamen University, Xiamen 361005, China (e-mail: feng.han@gbu.edu.cn; feng.han@xmu.edu.cn).

Digital Object Identifier 10.1109/TMTT.2026.3663207

I. Introduction

ELECTROMAGNETIC (EM) scattering is defined as the process by which EM waves interact with targets immersed inside an ambient medium and having different dielectric parameters, resulting in changes in wave propagation direction, amplitudes, phases, polarization, etc. [1]. Due to its wide applications in both military and civil areas, such as unidentified flying target tracking [2], unexploded land mine detection [3], security checks of concealed weapons [4], pavement distress inspection [5], and geophysical exploration [6], fast and reliable methods used to accurately compute the scattered EM fields at the receiver array have always been research highlights in recent years.

The most commonly used method to solve EM scattering is using integral equations (IEs), which are formulated under the framework of equivalence principles. The total EM fields are expressed as the summation of incident fields when the scatterers are absent and the scattered fields radiated by the fictitious equivalent currents, which are in turn proportional to the unknown total EM fields [7]. This closed process is mathematically formulated by the Fredholm IE. [8]. For penetrable inhomogeneous scatterers, volume IEs (VIEs) must be used [9]. However, surface IEs (SIEs) are the preferred choices for highly conductive or homogeneous dielectric scatterers [10]. Since IEs usually have no analytical solution, numerous numerical methods have been developed. The most typical one is the method of moment (MoM) [11]. It is realized by discretizing the whole computational domain into a series of arc, triangle, quadrilateral, tetrahedral, or hexahedral elements, using basis functions such as roof-top, Rao–Wilton–Glisson (RWG), or Schaubert–Wilton–Glisson (SWG) conformal with the element shapes to represent the unknown total EM fields or equivalent currents, sampling the IEs using testing functions so as to transform them into algebra equations, and finally solving them using direct matrix inverse or iterative algorithms [12], [13], [14]. The traditional MoM has the obvious merit of strong adaptability. It can be used to solve EM scattering from objects with arbitrary shapes since the RWG or the SWG is a subdomain basis function (SDBF). However, this also leads to the obvious drawback of MoM. Because the SDBF is only

capable of formulating the EM fields in a small local region, a minimum sampling density (SD) of 10 points per wavelength (PPW) is required to discretize the computational domain. Violating this rule of thumb will lead to a dramatic decrease in computation accuracy. Consequently, a huge number of freedoms are generated to deal with EM scattering from objects with large electrical sizes, which leads to a tremendous computational cost. Although some fast algorithms such as the stabilized biconjugate gradient FFT (BCGS-FFT) [15], the adaptive integral method (AIM) [16], and the multilevel fast multipole algorithm (MLFMA) [17] are used to lower the computational cost, calculating EM scattering from scatterers with large electrical sizes remains a significant burden.

In sharp contrast to the MoM applied to EM scattering from objects with arbitrary shapes, the mode-matching methods, such as the Mie series [18], have extremely high efficiencies to deal with EM scattering from objects with perfect canonical geometries, such as a closed standard sphere or a closed circular cylinder. In this situation, IEs become unnecessary. All the EM fields, including incident, scattered, and total fields, are directly expanded by the Fourier series or the spherical harmonics since they have obvious periodicity on the surface of the scatterer. Then, the coefficients of the unknowns, such as total fields or surface currents, are directly solved by independently matching the boundary condition for each harmonic mode on the scatterer surface. Compared with the traditional MoM, this mode-matching method has extreme superiority in the computational cost. However, its adaptability is too weak. The scatterers must have perfect canonical geometries, which is far from the real-world situation.

The spectral integral method (SIM) compromises the method of SIE and the mode-matching method by implementing the integration in the spectral domain. It can adapt to scatterers slightly deviating away from the perfect canonical geometries but still maintains a high computation efficiency. In the past decades, two kinds of SIM realization have been reported. The first one is achieved with the help of the entire-domain basis function (EDBF) and is mainly used in the computation of surface currents of antennas having the partially or nonclosed canonical geometries, e.g., 2-D circular disks or 3-D spherical caps. In this situation, the equivalent current flowing on the antenna surface is smooth with the variation in the wavelength scale. Using the EDBF instead of the SDBF in IEs can significantly reduce the number of basis functions to represent the current distribution, leading to a remarkable decrease in the computational cost. Meanwhile, because the antenna in a certain direction, e.g., $\hat{\theta}$ or $\hat{\phi}$, has the full or partial canonical geometry, the EDBF can be fully or partially represented by Fourier series or spherical harmonics. Therefore, retaining the unknown coefficients of the EDBF in the original IEs but using the Galerkin method in the spectral domain to assemble the impedance matrix of MoM and simultaneously testing the source term using EDBF represented by spherical harmonics, which is the core idea of SIM, can further save the computation cost. Typical applications of this kind of SIM include the optimized design of a large-scale metasurface [19], evaluation of the resonant frequency of microstrip structures [20], computation of the input impedance of a spherical microstrip antenna [21], analysis of microstrip antenna arrays mounted on a sphere surface [22], etc.

Hu proposed another different realization of SIM in [23] which is mainly used to compute EM scattering from arbitrarily smooth but closed 2-D cylinders. It discards the EDBF and the Galerkin method and directly leverages the ideas of the Mie series. Due to the periodicity of the EM fields on the arbitrarily smooth but closed boundary, the unknown total fields and Green's functions on the boundary are directly expanded by Fourier series. Therefore, the original convolutional integral in the SIE is transformed into the multiplication of coefficients of Fourier series of unknown total fields and Green's functions. Then, the continuous equation is tested by Dirac delta functions in the spatial domain to form the final discretized matrix equation in which the unknown vector consists of the Fourier coefficients of the surface currents with different orders, but the source term remains in the spatial domain. Because the SIM in [23] uses the spectral-domain basis functions to represent the unknowns, it can break the restriction of SD of 10 PPW in the traditional SIE. Theoretically speaking, an SD of 10 PPW is able to guarantee the computation accuracy according to the Nyquist sampling theorem. Therefore, the SIM proposed in [23] has been applied in several fields including fast computation of EM scattering from multilayer isotropic or anisotropic material [24], [25], efficient hybridization with spectral element method (SEM) [26], [27], etc.

In this work, we extend the SIM proposed in [23] and tested in [24], [25], [26], and [27] to the computation of EM scattering from smooth and closed 3-D objects. In particular, we first only exercise SIM on a smooth sphere with its center located at the origin. The smooth equivalent surface currents in the SIE are represented by a finite number of terms of vector spherical harmonics (VSH) [28], [29]. Their coefficients are unknowns to be solved by SIM. Meanwhile, the integration of the multiplication of the VSH and 3-D dyadic Green's functions (DGFs) can be treated as their spherical harmonic expansions, which fortunately have analytical expressions. The singularity of DGFs actually is manifested by the infinite number of expansion terms. Therefore, without applying the similar singularity extraction technique discussed in [23], the SIE for 3-D EM scattering from a sphere can be transformed into the SIM equation in which the VSH coefficients of surface currents and DGFs are multiplied. DGFs' infinite VSH expansion terms are automatically truncated by the finite number of VSH expansion terms of the smooth surface currents. Details will be discussed in Section II. Note this SIM is different from the Mie series since it originates from the traditional SIE and thus is built to deal with more general EM scattering problems, e.g., scatterers with arbitrary smooth boundaries. It is a complete imitation of that proposed in [23] and is ready to extend to a 3-D scatterer with a general smooth shape, e.g., an ellipsoid, which will be discussed in Section IV.

This article is organized as follows. In Section II, the conventional spatial-domain 3-D electric field IE (EFIE) for EM scattering from a metal sphere and the Poggio–Miller–Chang–Harrington–Wu–Tsai (PMCHWT)

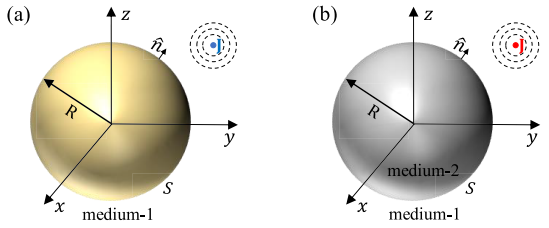

Fig. 1. (a) Metal sphere and (b) dielectric sphere with the radii of R and immersed in medium-1 are illuminated by EM waves excited by infinitesimal electric dipoles.

equations for EM scattering from a dielectric one are first given. They are then transformed into the spectral-domain EFIE and PMCHWT equations by expanding both the equivalent surface currents and DGFs using the VSH series. Discretization and assemblies of the algebraic system matrices as well as radiation ones are discussed. In Section III, two numerical examples are given to validate the reliability, correctness, efficiency, and cost of SIM for computing EM scattering from a smooth metal sphere and a dielectric sphere by comparing its results with those from the traditional MoM as well as the commercial software Altair Feko. In addition, the quantitative relationship between the required number of VSH modes to accurately represent the scattered fields and the source distance from the scatterer is also investigated by numerical simulations. Section IV presents the summary, conclusion, and future work.

II. Formulation

In this section, the conventional spatial-domain surface EFIE and PMCHWT equations based on DGFs are first given. The corresponding compact operators are formulated. Then, by expanding both the smooth equivalent currents and the DGFs on the closed sphere surface with the VSH series, we obtain the spectral-domain EFIE and PMCHWT equations, which also can be represented by compact operators. Finally, they are discretized through sampling the EM field values on a series of perturbed spherical Fibonacci grids (SFGs). The matrix-form equations are formed by forcing the number of discrete field points to coincide with the order of the VSH series.

A. Spatial-Domain EFIE and PMCHWT Equations

As shown in Fig. 1(a), a metal sphere with a radius of R and its center located at the origin is illuminated by a 3-D infinitesimal electric dipole. Since the tangential electric fields are zero on the metal sphere surface S, the N-type surface EFIE can be constructed as follows:

$$-\hat{n}\times\mathbf{E}^{inc}(\mathbf{r}) = \hat{n}\times\frac{1}{\eta_0}\oint_S \overline{\overline{\mathbf{G}}}^{1}_{\mathbf{EJ}}(\mathbf{r},\mathbf{r}')\cdot\bar{\mathbf{J}}(\mathbf{r}')\,dS' \tag{1}$$

where η_0 is the intrinsic impedance in the free space, $\bar{\mathbf{J}} = \eta_0\mathbf{J}$ is the scaled equivalent surface electric current density, $\hat{n}$ is the outward normal unit vector on S, $\oint$ is the Cauchy principal integral used to circumvent the singularity when the source point $\mathbf{r}'$ and the field point $\mathbf{r}$ overlap on S, the superscript 1 denotes the medium-1, and $\overline{\overline{\mathbf{G}}}^{1}_{\mathbf{EJ}}$ is the 3-D DGF which is constructed as follows:

$$\overline{\overline{\mathbf{G}}}^{1}_{\mathbf{EJ}} = -j\omega\mu_1\mu_0\overline{\overline{\mathbf{G}}}^{1}_{e} = -j\omega\mu_1\mu_0\left[1+\frac{\nabla\nabla}{k_1^2}\right]\left[\bar{\bar{\mathbf{I}}}g_1(\mathbf{r},\mathbf{r}')\right] \tag{2}$$

where μ_1 and k_1 are, respectively, the relative permeability and wavenumber of the background medium-1, and

$$g_1(\mathbf{r},\mathbf{r}') = \frac{\exp(-jk_1|\mathbf{r}-\mathbf{r}'|)}{4\pi|\mathbf{r}-\mathbf{r}'|} \tag{3}$$

is the 3-D scalar Green's function. Equation (1) can be rewritten in a compact form

$$-\hat{n}\times\mathbf{E}^{inc}(\mathbf{r}) = \hat{n}\times\frac{-j\omega\mu_1\mu_0}{\eta_0}\mathcal{L}_1\{\bar{\mathbf{J}}\} \tag{4}$$

where $\mathcal{L}_1\{\} = \oint_S \overline{\overline{\mathbf{G}}}^{1}_{e}\cdot\{\}dS'$ is the dyadic integral operator.

When the scatterer becomes a homogeneous dielectric sphere, as shown in Fig. 1(b), the N-type PMCHWT equations can be constructed as follows:

$$\begin{aligned}
&-\hat{n}\times\mathbf{E}^{inc}(\mathbf{r})\\
&=\hat{n}\times\frac{1}{\eta_0}\oint_S\left\{\overline{\overline{\mathbf{G}}}^{1}_{\mathbf{EJ}}(\mathbf{r},\mathbf{r}')+\overline{\overline{\mathbf{G}}}^{2}_{\mathbf{EJ}}(\mathbf{r},\mathbf{r}')\right\}\cdot\bar{\mathbf{J}}(\mathbf{r}')\,dS'\\
&\quad+\hat{n}\times\oint_S\left\{\overline{\overline{\mathbf{G}}}^{1}_{\mathbf{EM}}(\mathbf{r},\mathbf{r}')+\overline{\overline{\mathbf{G}}}^{2}_{\mathbf{EM}}(\mathbf{r},\mathbf{r}')\right\}\cdot\mathbf{M}(\mathbf{r}')\,dS' \qquad (5a)\\
&-\hat{n}\times\eta_0\mathbf{H}^{inc}(\mathbf{r})\\
&=\hat{n}\times\oint_S\left\{\overline{\overline{\mathbf{G}}}^{1}_{\mathbf{HJ}}(\mathbf{r},\mathbf{r}')+\overline{\overline{\mathbf{G}}}^{2}_{\mathbf{HJ}}(\mathbf{r},\mathbf{r}')\right\}\cdot\bar{\mathbf{J}}(\mathbf{r}')\,dS'\\
&\quad+\hat{n}\times\oint_S\left\{\eta_0\overline{\overline{\mathbf{G}}}^{1}_{\mathbf{HM}}(\mathbf{r},\mathbf{r}')+\eta_0\overline{\overline{\mathbf{G}}}^{2}_{\mathbf{HM}}(\mathbf{r},\mathbf{r}')\right\}\cdot\mathbf{M}(\mathbf{r}')\,dS' \qquad (5b)
\end{aligned}$$

where $\overline{\overline{\mathbf{G}}}^{1,2}_{\mathbf{EM}} = -\overline{\overline{\mathbf{G}}}^{1,2}_{\mathbf{HJ}} = -\nabla\times\bar{\bar{\mathbf{I}}}g_{1,2}(\mathbf{r},\mathbf{r}') = \overline{\overline{\mathbf{G}}}^{1,2}_{m}$ and $\overline{\overline{\mathbf{G}}}^{1,2}_{\mathbf{HM}} = -j\omega\epsilon_{1,2}\varepsilon_0\overline{\overline{\mathbf{G}}}^{1,2}_{e}$ are also 3-D DGFs, and $\mathbf{M}$ is the equivalent surface magnetic current density. Equation (5) can also be rewritten in a compact form, which is shown in (6) at the bottom of this page. In (6), $\mathcal{K}_{1,2} = \oint_S \overline{\overline{\mathbf{G}}}^{1,2}_{m}\cdot\{\}dS'$ are also dyadic integral operators. Once $\bar{\mathbf{J}}$ and $\mathbf{M}$ are solved for from (4) or (6), the scattered fields at the receiver array can be immediately evaluated still using the operators $\mathcal{L}$ and $\mathcal{K}$. The only difference is that the regular integral instead of the Cauchy principal integral is adopted in them since no singularity exists in this situation. Finally, it is worth mentioning that the operators $\mathcal{L}$ and $\mathcal{K}$ are defined using the 3-D DGFs instead of the scalar Green's function g in (3). In literature, the two operators based on the scalar Green's function g are widely used since they can be further simplified when acting on the RWG basis functions. However, they are usually defined using the 3-D DGFs when the background

$$\begin{bmatrix} -\hat{n}\times\mathbf{E}^{inc} \\ -\hat{n}\times\eta_0\mathbf{H}^{inc}\end{bmatrix} = \begin{bmatrix} \hat{n}\times\frac{-j\omega}{\eta_0}(\mu_1\mu_0\mathcal{L}_1+\mu_2\mu_0\mathcal{L}_2) & \hat{n}\times(\mathcal{K}_1+\mathcal{K}_2) \\ -\hat{n}\times(\mathcal{K}_1+\mathcal{K}_2) & -\hat{n}\times j\omega\eta_0(\epsilon_1\varepsilon_0\mathcal{L}_1+\epsilon_2\varepsilon_0\mathcal{L}_2)\end{bmatrix}\begin{bmatrix}\bar{\mathbf{J}}\\ \mathbf{M}\end{bmatrix} \tag{6}$$

medium is anisotropic or planarly stratified [30], [31] since the regular scalar Green's function g is not enough to express the EM radiation in these situations. In this work, we also use the 3-D DGFs to define $\mathcal{L}$ and $\mathcal{K}$ since they can be directly expanded using spherical harmonic series, which will be discussed in Section II-B.

B. SIM For EM Scattering From a 3-D Sphere

In the previous works [23], [25], [32], the unknown total fields on the smooth and closed cylindrical boundaries are expanded by the truncated Fourier series since they are periodic functions of the azimuthal angle with the cycle of 2π. In this work, the surface currents $\bar{\mathbf{J}}$ and $\mathbf{M}$ on the closed spheric surface are vectors instead of scalars. Meanwhile, they are periodic functions of the solid angle with the cycle of 4π. Therefore, we expand them using the VSH series instead of the scalar spherical harmonic (SSH) series. Note the specific mathematical expressions of VSH and SSH are given in (A1) and (A2) of Appendix. On the other hand, because we only consider a standard sphere with its center located at the origin in this work, the smooth tangential surface currents $\bar{\mathbf{J}}$ and $\mathbf{M}$ only have the $\hat{\theta}$- and $\hat{\phi}$-components. Therefore, they can be expanded by the truncated VSH series

$$\bar{\mathbf{J}}(\theta,\phi) = \sum_{l=1}^{L}\sum_{m=-l}^{l} a_l^m \mathbf{m}_l^m(\theta,\phi) + b_l^m \mathbf{n}_l^m(\theta,\phi) \tag{7a}$$

$$\mathbf{M}(\theta,\phi) = \sum_{l=1}^{L}\sum_{m=-l}^{l} c_l^m \mathbf{m}_l^m(\theta,\phi) + d_l^m \mathbf{n}_l^m(\theta,\phi) \tag{7b}$$

in which a_l^m, b_l^m, c_l^m, and d_l^m are the unknown coefficients to be solved, and l and m are the orders of the VSH series. We then redefine the integral on the sphere surface $\int_S \{\} dS' = \int_0^{2\pi}\int_0^{\pi}\{\} r'^2 \sin\theta' d\theta' d\phi'$, apply the operators $\mathcal{L}$ and $\mathcal{K}$ to the surface current density $\bar{\mathbf{J}}$ and $\mathbf{M}$ in (7), exchange the order of summation and integration, and, finally, construct the spectral-domain operators as follows:

$$\widetilde{\mathcal{L}}\{\bar{\mathbf{J}}\} = \sum_{l=1}^{L}\sum_{m=-l}^{l} a_l^m \int_0^{2\pi}\int_0^{\pi} \overline{\overline{\mathbf{G}}}_e \cdot \mathbf{m}_l^m r'^2 \sin\theta' d\theta' d\phi' + \sum_{l=1}^{L}\sum_{m=-l}^{l} b_l^m \int_0^{2\pi}\int_0^{\pi} \overline{\overline{\mathbf{G}}}_e \cdot \mathbf{n}_l^m r'^2 \sin\theta' d\theta' d\phi' \tag{8a}$$

$$\widetilde{\mathcal{L}}\{\mathbf{M}\} = \sum_{l=1}^{L}\sum_{m=-l}^{l} c_l^m \int_0^{2\pi}\int_0^{\pi} \overline{\overline{\mathbf{G}}}_e \cdot \mathbf{m}_l^m r'^2 \sin\theta' d\theta' d\phi' + \sum_{l=1}^{L}\sum_{m=-l}^{l} d_l^m \int_0^{2\pi}\int_0^{\pi} \overline{\overline{\mathbf{G}}}_e \cdot \mathbf{n}_l^m r'^2 \sin\theta' d\theta' d\phi' \tag{8b}$$

$$\widetilde{\mathcal{K}}\{\bar{\mathbf{J}}\} = \sum_{l=1}^{L}\sum_{m=-l}^{l} a_l^m \int_0^{2\pi}\int_0^{\pi} \overline{\overline{\mathbf{G}}}_m \cdot \mathbf{m}_l^m r'^2 \sin\theta' d\theta' d\phi' + \sum_{l=1}^{L}\sum_{m=-l}^{l} b_l^m \int_0^{2\pi}\int_0^{\pi} \overline{\overline{\mathbf{G}}}_m \cdot \mathbf{n}_l^m r'^2 \sin\theta' d\theta' d\phi' \tag{8c}$$

$$\widetilde{\mathcal{K}}\{\mathbf{M}\} = \sum_{l=1}^{L}\sum_{m=-l}^{l} c_l^m \int_0^{2\pi}\int_0^{\pi} \overline{\overline{\mathbf{G}}}_m \cdot \mathbf{m}_l^m r'^2 \sin\theta' d\theta' d\phi' + \sum_{l=1}^{L}\sum_{m=-l}^{l} d_l^m \int_0^{2\pi}\int_0^{\pi} \overline{\overline{\mathbf{G}}}_m \cdot \mathbf{n}_l^m r'^2 \sin\theta' d\theta' d\phi' \tag{8d}$$

where $\overline{\overline{\mathbf{G}}}_e = \overline{\overline{\mathbf{G}}}_e(r,\theta,\phi,r',\theta',\phi')$, $\overline{\overline{\mathbf{G}}}_m = \overline{\overline{\mathbf{G}}}_m(r,\theta,\phi,r',\theta',\phi')$, $\mathbf{m}_l^m = \mathbf{m}_l^m(\theta',\phi')$, and $\mathbf{n}_l^m = \mathbf{n}_l^m(\theta',\phi')$. Because the center of the sphere is located at the origin, $r'^2 = R^2$ in (8) is a constant with respect to the variations of θ' and ϕ', and thus can be moved outside of the double integral. Consequently, the double integral actually becomes evaluating the vectorial coefficient of the VSH expansion of $\overline{\overline{\mathbf{G}}}_e$ or $\overline{\overline{\mathbf{G}}}_m$ using the basis $\mathbf{m}_l^{m*}$ or $\mathbf{n}_l^{m*}$ in the solid angle θ'-ϕ' space. Here, the superscript $*$ denotes the complex conjugate. The luckiest thing is that $\overline{\overline{\mathbf{G}}}_e$ and $\overline{\overline{\mathbf{G}}}_m$ can be expanded using the dyadics of $\mathbf{l}_l^m$, $\mathbf{m}_l^m$, or $\mathbf{n}_l^m$ and their complex conjugates. The specific analytical expressions are given in (A4a) and (A4b) of Appendix. Therefore, (8) can be further simplified as follows:

$$\widetilde{\mathcal{L}}\{\bar{\mathbf{J}}\} = \sum_{l=1}^{L}\sum_{m=-l}^{l} a_l^m R^2 u_l^1 \mathbf{m}_l^m + b_l^m R^2 u_l^2 \mathbf{n}_l^m + b_l^m R^2 u_l^3 \mathbf{l}_l^m \tag{9a}$$

$$\widetilde{\mathcal{L}}\{\mathbf{M}\} = \sum_{l=1}^{L}\sum_{m=-l}^{l} c_l^m R^2 u_l^1 \mathbf{m}_l^m + d_l^m R^2 u_l^2 \mathbf{n}_l^m + d_l^m R^2 u_l^3 \mathbf{l}_l^m \tag{9b}$$

$$\widetilde{\mathcal{K}}\{\bar{\mathbf{J}}\} = \sum_{l=1}^{L}\sum_{m=-l}^{l} a_l^m R^2 v_l^1 \mathbf{n}_l^m + a_l^m R^2 v_l^2 \mathbf{l}_l^m + b_l^m R^2 v_l^3 \mathbf{m}_l^m \tag{9c}$$

$$\widetilde{\mathcal{K}}\{\mathbf{M}\} = \sum_{l=1}^{L}\sum_{m=-l}^{l} c_l^m R^2 v_l^1 \mathbf{n}_l^m + c_l^m R^2 v_l^2 \mathbf{l}_l^m + d_l^m R^2 v_l^3 \mathbf{m}_l^m \tag{9d}$$

where the coefficients are

$$u_l^1 = -jk h_l^{(2)}(kR)\, j_l(kR) \tag{10a}$$

$$u_l^2 = -\frac{j}{kR^2}\left[\frac{\partial\left(r h_l^{(2)}(kr)\right)}{\partial r}\frac{\partial\left(r j_l(kr)\right)}{\partial r}\right]_{r=R} \tag{10b}$$

$$u_l^3 = -\frac{j\sqrt{l(l+1)}}{2kR^2}\left[h_l^{(2)}(kr)\frac{\partial\left(r j_l(kr)\right)}{\partial r}\right]_{r=R} - \frac{j\sqrt{l(l+1)}}{2kR^2}\left[j_l(kr)\frac{\partial\left(r h_l^{(2)}(kr)\right)}{\partial r}\right]_{r=R} \tag{10c}$$

$$v_l^1 = \frac{jk}{2R}\left[j_l(kr)\frac{\partial\left(r h_l^{(2)}(kr)\right)}{\partial r} + h_l^{(2)}(kr)\frac{\partial\left(r j_l(kr)\right)}{\partial r}\right]_{r=R} \tag{10d}$$

$$\begin{bmatrix} E_\phi^{inc} \\ -E_\theta^{inc} \\ \eta_0 H_\phi^{inc} \\ -\eta_0 H_\theta^{inc} \end{bmatrix} = R^2 \sum_{l=1}^{L}\sum_{m=-l}^{l} \frac{1}{\sqrt{l(l+1)}} \begin{bmatrix} -s_l^1 \frac{\partial Y_l^m}{\partial\theta} & s_l^2 \frac{1}{\sin\theta}\frac{\partial Y_l^m}{\partial\phi} & -t_l^1 \frac{1}{\sin\theta}\frac{\partial Y_l^m}{\partial\phi} & t_l^3 \frac{\partial Y_l^m}{\partial\theta} \\ -s_l^1 \frac{1}{\sin\theta}\frac{\partial Y_l^m}{\partial\phi} & -s_l^2 \frac{\partial Y_l^m}{\partial\theta} & t_l^1 \frac{\partial Y_l^m}{\partial\theta} & t_l^3 \frac{1}{\sin\theta}\frac{\partial Y_l^m}{\partial\phi} \\ t_l^1 \frac{1}{\sin\theta}\frac{\partial Y_l^m}{\partial\phi} & -t_l^3 \frac{\partial Y_l^m}{\partial\theta} & -w_l^1 \frac{\partial Y_l^m}{\partial\theta} & w_l^2 \frac{1}{\sin\theta}\frac{\partial Y_l^m}{\partial\phi} \\ -t_l^1 \frac{\partial Y_l^m}{\partial\theta} & -t_l^3 \frac{1}{\sin\theta}\frac{\partial Y_l^m}{\partial\phi} & -w_l^1 \frac{1}{\sin\theta}\frac{\partial Y_l^m}{\partial\phi} & -w_l^2 \frac{\partial Y_l^m}{\partial\theta} \end{bmatrix} \begin{bmatrix} a_l^m \\ b_l^m \\ c_l^m \\ d_l^m \end{bmatrix} \tag{12}$$

$$v_l^2 = \frac{jk\sqrt{l(l+1)}}{R} h_l^{(2)}(kR)\, j_l(kR) \tag{10e}$$

$$v_l^3 = v_l^1. \tag{10f}$$

Finally, by leveraging the identities $\hat{n} \times \hat{\theta} = \hat{r} \times \hat{\theta} = \hat{\phi}$, $\hat{n} \times \hat{\phi} = -\hat{\theta}$, and $\hat{n} \times \mathbf{l}_l^m = 0$, substituting the spectral-domain operators in (9) into (4) and (6), respectively, substituting $\bar{\mathbf{J}}$ and $\mathbf{M}$ defined in (7) into (4) and (6), respectively, and detaching the $\hat{\theta}$- and $\hat{\phi}$-components, we, respectively, obtain the spectral-domain EFIE for EM scattering from a metal sphere with its center located at the origin as follows:

$$\begin{bmatrix} E_\phi^{inc} \\ -E_\theta^{inc} \end{bmatrix} = \frac{-j\omega\mu_1\mu_0 R^2}{\eta_0} \sum_{l=1}^{L} \sum_{m=-l}^{l} \frac{1}{\sqrt{l(l+1)}} \cdot \begin{bmatrix} u_{l,1}^1 \frac{\partial Y_l^m}{\partial \theta} & -u_{l,1}^2 \frac{1}{\sin\theta} \frac{\partial Y_l^m}{\partial \phi} \\ u_{l,1}^1 \frac{1}{\sin\theta} \frac{\partial Y_l^m}{\partial \phi} & u_{l,1}^2 \frac{\partial Y_l^m}{\partial \theta} \end{bmatrix} \begin{bmatrix} a_l^m \\ b_l^m \end{bmatrix} \tag{11}$$

and the spectral-domain PMCHWT equations for EM scattering from a dielectric sphere with its center located at the origin, which are shown in (12) at the bottom of the previous page, where

$$\begin{cases} s_l^1 = \dfrac{j\omega\mu_0}{\eta_0}\left(\mu_1 u_{l,1}^1 + \mu_2 u_{l,2}^1\right) \\ s_l^2 = \dfrac{j\omega\mu_0}{\eta_0}\left(\mu_1 u_{l,1}^2 + \mu_2 u_{l,2}^2\right) \\ t_l^1 = v_{l,1}^1 + v_{l,2}^1,\ t_l^3 = v_{l,1}^3 + v_{l,2}^3 \\ w_l^1 = j\omega\eta_0\varepsilon_0\left(\epsilon_1 u_{l,1}^1 + \epsilon_2 u_{l,2}^1\right) \\ w_l^2 = j\omega\eta_0\varepsilon_0\left(\epsilon_1 u_{l,1}^2 + \epsilon_2 u_{l,2}^2\right) \end{cases} \tag{13}$$

in which the second subscripts of $u_{l,1}^1$, $u_{l,2}^1$, $u_{l,1}^2$, $u_{l,2}^2$, $v_{l,1}^1$, $v_{l,2}^1$, $v_{l,1}^3$, and $v_{l,2}^3$ denote the medium index in which u_l^1, u_l^2, v_l^1, and v_l^3 given in (10) are evaluated. For example, $u_{l,2}^2$ is computed using (10b) with the wavenumber k taking the value in the medium-2 (inside the sphere). Four points must be emphasized here. First, (11) and (12) are the 3-D spectral integral equations for EM scattering from a sphere with its center located at the origin. The operation of the double summation corresponds to the original double integral in the SIE. The coefficients a_l^m, b_l^m, c_l^m, and d_l^m are the unknowns to be determined. Second, (11) and (12) stay in the continuous states. Not only the incidents fields E_θ^{inc}, E_ϕ^{inc}, H_θ^{inc}, and H_ϕ^{inc} continuously vary with θ and ϕ but also the SSH Y_l^m varies with θ and ϕ. Therefore, the discretization is necessary to solve for the unknowns a_l^m, b_l^m, c_l^m, and d_l^m, and this will be discussed in Section II-C. Third, as mentioned in Appendix, $\overline{\overline{\mathbf{G}}}_e$ and $\overline{\overline{\mathbf{G}}}_m$ have singularities when $r = r' = R$. This leads to an infinite number of VSH expansion terms. However, the VSH expansions of $\bar{\mathbf{J}}$ and $\mathbf{M}$ have a finite number of terms, which can automatically truncate the expansions of $\overline{\overline{\mathbf{G}}}_e$ and $\overline{\overline{\mathbf{G}}}_m$ without losing computation accuracy. Fourth, once the coefficients a_l^m, b_l^m, c_l^m, and d_l^m are solved for from (11) and (12), the scattered fields at the receiver array can be evaluated by still using the operators $\widetilde{\mathcal{L}}$ and $\widetilde{\mathcal{K}}$ defined in (9). However, because the field point is located at the receiver array, the coefficients given in (10) must modified as follows:

$$u_{l,1}^1 = -jk_1 h_l^{(2)}(k_1 R_r)\, j_l(k_1 R) \tag{14a}$$

$$u_{l,1}^2 = \frac{-j}{k_1 R_r R}\left[\frac{\partial\left(r h_l^{(2)}(k_1 r)\right)}{\partial r}\right]_{r=R_r} \times \left[\frac{\partial\left(r j_l(k_1 r)\right)}{\partial r}\right]_{r=R} \tag{14b}$$

$$u_{l,1}^3 = -\frac{j\sqrt{l(l+1)}}{k_1 R R_r} h_l^{(2)}(k_1 R_r)\left[\frac{\partial\left(r j_l(k_1 r)\right)}{\partial r}\right]_{r=R} \tag{14c}$$

$$v_{l,1}^1 = \frac{jk_1}{R_r} j_l(k_1 R)\left[\frac{\partial\left(r h_l^{(2)}(k_1 r)\right)}{\partial r}\right]_{r=R_r} \tag{14d}$$

$$v_{l,1}^2 = \frac{jk_1\sqrt{l(l+1)}}{R_r} h_l^{(2)}(k_1 R_r)\, j_l(k_1 R) \tag{14e}$$

$$v_{l,1}^3 = \frac{jk_1}{R} h_l^{(2)}(k_1 R_r)\left[\frac{\partial\left(r j_l(kr)\right)}{\partial r}\right]_{r=R} \tag{14f}$$

where R_r is the radial coordinate of the rth receiver. Meanwhile, the variables (θ, ϕ) of $\mathbf{l}_l^m$, $\mathbf{m}_l^m$, and $\mathbf{n}_l^m$ must be changed to (θ_r, ϕ_r) which is the angular coordinate of the rth receiver.

C. Discretization of the 3-D Spectral IEs

Equations (11) and (12) vary continuously with the field point (θ, ϕ) on the sphere surface. However, there are a total of $2M$ unknown coefficients in (11) and $4M$ unknown coefficients in (12) with $M = (L+1)^2 - 1$. Therefore, it is necessary to sample M sets of discrete (θ, ϕ) values on the sphere surface to generate $2M$ groups of equations from (11) and $4M$ groups of equations from (12). Theoretically speaking, these discrete field points can be picked on the sphere surface without restriction as long as they can be used to form the $2M$ or $4M$ equations. However, randomly choosing these field points may lead to a strong correlation between the rows or columns of the system matrix, which will enlarge its ill-posedness and thus finally compromise the reliability of the solution. In the previous works [24], [25] for 2-D SIM, the field points on the circular or elliptical circumference are picked with an equal interval of the azimuthal angle. Indeed, the system matrix of the 2-D SIM is composed of the Fourier basis $e^{-jm\phi}$. Sampling the field points on the circumference with the equal $\Delta\phi$ can effectively avoid the correlation of the rows or columns of the system matrix by leveraging the orthogonality of the Fourier basis $e^{-jm\phi}$, and thus significantly lower the condition number of the system matrix.

In this work, for the 3-D SIM, we try six sampling schemes. The first scheme is to randomly pick M sets of (θ, ϕ) values. They are

$$\begin{cases} \theta_i = \text{rand}(0, \pi) \\ \phi_i = \text{rand}(0, 2\pi) \end{cases} \tag{15}$$

where $i \in [1, M]$ and $\text{rand}(a, b)$ is the operation to generate a random real number between a and b. The second scheme is the same as that in the 2-D SIM. Both the polar angle θ and the azimuthal angle ϕ are divided with equal intervals and are mathematically expressed as follows:

$$\begin{cases} \theta_i = \dfrac{\pi(i - 0.5)}{L} \\ \phi_j = \dfrac{2\pi(j - 0.5)}{L+2} \end{cases} \tag{16}$$

where $i \in [1, L]$ and $j \in [1, L+2]$. In the third scheme, we use the SFG suggested in [33]. The sampling points are picked according to

$$\begin{cases} \theta_i = \arccos\left(1 - \dfrac{2i-1}{M}\right) \\ \phi_i = i\Delta\phi \bmod 2\pi \end{cases} \tag{17}$$

where $i \in [1, M]$, $\Delta\phi = 2\pi \times (\sqrt{5}-1)/2$ is selected according to the golden ratio, and mod is the modulo operation. On one hand, the SFG can yield the extremely uniform sampling points on the sphere. This suppresses the possible correlation of the rows or columns of the system matrix to the maximum extent. On the other hand, $\Delta\phi$ is selected according to the golden ratio number $(\sqrt{5}-1)/2$ which is the most difficult irrational number to approximate with fractions. This guarantees the chaos of the sampling points on the sphere surface, avoids their regular arrangement, and thus further reduces the correlation of the rows or columns of the system matrix. The fourth and fifth schemes are similar to the third one but the increment interval is adjusted to $\Delta\phi = 2\pi \times 0.617$ and $\Delta\phi = 2\pi \times 0.619$, respectively. The purpose of these two schemes is to verify how the condition number of the system matrix is significantly altered by a rational number approaching the golden ratio number. An increment interval based on a rational number easily leads to the alignment of those discrete points along the lines of latitude and longitude, generating an almost regular arrangement. The sixth scheme is also similar to the third one but with a small random perturbation added to the ϕ value of each sampling point on the sphere surface. Therefore, we first use (17) to compute the angular coordinates of all the sampling points. Then, ϕ_i is updated by the following equation:

$$\phi_i^2 = \phi_i + \text{rand}\,(0, \Phi) - 0.5\Phi \tag{18}$$

where $\Phi = \min_{\substack{1 \le i,j \le M \\ i \ne j}} |\phi_i - \phi_j|$, and ϕ_i^2 is the true value used in the sixth scheme. This controlled randomness imposed upon the traditional SFG is expected to further reduce the correlation of the discrete points on the sphere surface. The condition numbers of the system matrices for all these six schemes with different sampling densities are compared. Details are shown in Section III. It is found that the sixth scheme generates the lowest condition number for both the discretized spectral-domain EFIE and PMCHWT equations. Therefore, the sixth scheme is adopted to discretize (11) and (12) to obtain their own system matrices, which are further used to compute the surface currents and scattered fields.

D. Assembly of the Algebraic System Matrix

Once (11) is discretized using the M sets of field data on the sphere surface, it can be compactly written as follows:

$$\mathbf{V} = \mathbf{Z}\mathbf{I} = [\mathbf{Z}_a \quad \mathbf{Z}_b]\,\mathbf{I} \tag{19}$$

where $\mathbf{V} \in \mathbb{C}^{2M\times 1}$, $\mathbf{Z} \in \mathbb{C}^{2M\times 2M}$, $\mathbf{Z}_{a,b} \in \mathbb{C}^{2M\times M}$, and $\mathbf{I} \in \mathbb{C}^{2M\times 1}$. They are assembled as follows:

$$\mathbf{V} = \left[\mathbf{V}^1 \cdots \mathbf{V}^i \cdots \mathbf{V}^M\right]^T \tag{20a}$$

$$\mathbf{Z}_{a,b} = \begin{bmatrix} \mathbf{Z}_{a,b}^{1,1} & \cdots & \mathbf{Z}_{a,b}^{1,l} & \cdots & \mathbf{Z}_{a,b}^{1,L} \\ \vdots & \ddots & & & \vdots \\ \mathbf{Z}_{a,b}^{i,1} & & \mathbf{Z}_{a,b}^{i,l} & & \mathbf{Z}_{a,b}^{i,L} \\ \vdots & & & \ddots & \vdots \\ \mathbf{Z}_{a,b}^{M,1} & \cdots & \mathbf{Z}_{a,b}^{M,l} & \cdots & \mathbf{Z}_{a,b}^{M,L} \end{bmatrix} \tag{20b}$$

$$\mathbf{I} = \left[\mathbf{a}^1 \cdots \mathbf{a}^l \cdots \mathbf{a}^L \cdots \mathbf{b}^1 \cdots \mathbf{b}^l \cdots \mathbf{b}^L\right]^T \tag{20c}$$

in which the superscript T denotes the matrix transpose. The submatrices are assembled as follows:

$$\mathbf{V}^i = \left[E_\phi^{inc}(\theta_i, \phi_i) \quad -E_\theta^{inc}(\theta_i, \phi_i)\right] \in \mathbb{C}^{1\times 2} \tag{21a}$$

$$\mathbf{Z}_{a,b}^{i,l} = \left[\mathbf{Z}_{a,b}^{i,-l} \cdots \mathbf{Z}_{a,b}^{i,m} \cdots \mathbf{Z}_{a,b}^{i,l}\right] \in \mathbb{C}^{2\times(2l+1)} \tag{21b}$$

$$\mathbf{a}^l = \left[a_l^{-l} \cdots a_l^m \cdots a_l^l\right] \in \mathbb{C}^{1\times(2l+1)} \tag{21c}$$

$$\mathbf{b}^l = \left[b_l^{-l} \cdots b_l^m \cdots b_l^l\right] \in \mathbb{C}^{1\times(2l+1)} \tag{21d}$$

where

$$\mathbf{Z}_a^{i,m} = \frac{-j\omega\mu_1\mu_0 R^2}{\eta_0\sqrt{l(l+1)}} \begin{bmatrix} u_{l,1}^1 \dfrac{\partial Y_l^m}{\partial\theta} \\ u_{l,1}^1 \dfrac{1}{\sin\theta}\dfrac{\partial Y_l^m}{\partial\phi} \end{bmatrix}_{\theta=\theta_i,\phi=\phi_i} \tag{22a}$$

$$\mathbf{Z}_b^{i,m} = \frac{-j\omega\mu_1\mu_0 R^2}{\eta_0\sqrt{l(l+1)}} \begin{bmatrix} -u_{l,1}^2 \dfrac{1}{\sin\theta}\dfrac{\partial Y_l^m}{\partial\phi} \\ u_{l,1}^2 \dfrac{\partial Y_l^m}{\partial\theta} \end{bmatrix}_{\theta=\theta_i,\phi=\phi_i} \tag{22b}$$

in which $i \in [1, M]$ and $m \in [-l, l]$. The $\mathbf{Z}$ in (19) is the system matrix of 3-D SIM for EM scattering from a metal sphere, and it is also called the spectral-domain impedance matrix. The system matrix of 3-D SIM for EM scattering from a dielectric sphere can be assembled similarly based on (12). When discretized, it can be compactly written as follows:

$$\mathbf{V} = \begin{bmatrix} \mathbf{V}^E \\ \mathbf{V}^H \end{bmatrix} = \mathbf{Z}\mathbf{I} = \begin{bmatrix} \mathbf{Z}_a^E & \mathbf{Z}_b^E & \mathbf{Z}_c^E & \mathbf{Z}_d^E \\ \mathbf{Z}_a^H & \mathbf{Z}_b^H & \mathbf{Z}_c^H & \mathbf{Z}_d^H \end{bmatrix} \mathbf{I} \tag{23}$$

where $\mathbf{V} \in \mathbb{C}^{4M\times 1}$, $\mathbf{V}^{E,H} \in \mathbb{C}^{2M\times 1}$, $\mathbf{Z} \in \mathbb{C}^{4M\times 4M}$, $\mathbf{Z}_{a,b,c,d}^{E,H} \in \mathbb{C}^{2M\times M}$, and $\mathbf{I} \in \mathbb{C}^{4M\times 1}$. The assembly of $\mathbf{V}^E$ is the same as that of $\mathbf{V}$ in (20a). The assembly of $\mathbf{V}^H$ is similar but with the incident magnetic fields used. The assembly of $\mathbf{I}$ is similar to that in (20c) but with the vectors including c_l^m and d_l^m cascaded. $\mathbf{Z}_{a,b,c,d}^E$ is assembled from elements in the first two rows of the continuous system matrix shown in (12), while $\mathbf{Z}_{a,b,c,d}^H$ is assembled from elements in the last two rows. The assembly of each submatrix of $\mathbf{Z}$ in (23) is similar to that given in (20b), (21b), and (22). For example, an element of $\mathbf{Z}_c^H$ can be constructed as follows:

$$\mathbf{Z}_c^{H,i,m} = \frac{R^2}{\sqrt{l(l+1)}} \begin{bmatrix} -w_l^1 \dfrac{\partial Y_l^m}{\partial\theta} \\ -w_l^1 \dfrac{1}{\sin\theta}\dfrac{\partial Y_l^m}{\partial\phi} \end{bmatrix}_{\theta=\theta_i,\phi=\phi_i} \tag{24}$$

in which $i \in [1, M]$ and $m \in [-l, l]$.

Once $\mathbf{I}$ is obtained from (19), the scattered fields at the receiver array can be computed using

$$\begin{bmatrix} \mathbf{E}_r^{sct} \\ \mathbf{E}_\theta^{sct} \\ \mathbf{E}_\phi^{sct} \end{bmatrix} = \begin{bmatrix} \mathbf{R}_r^E \\ \mathbf{R}_\theta^E \\ \mathbf{R}_\phi^E \end{bmatrix} \mathbf{I}, \quad \begin{bmatrix} \mathbf{H}_r^{sct} \\ \mathbf{H}_\theta^{sct} \\ \mathbf{H}_\phi^{sct} \end{bmatrix} = \begin{bmatrix} \mathbf{R}_r^H \\ \mathbf{R}_\theta^H \\ \mathbf{R}_\phi^H \end{bmatrix} \mathbf{I} \tag{25}$$

where the radiation matrices $\mathbf{R}_r^E$, $\mathbf{R}_\theta^E$, $\mathbf{R}_\phi^E$, $\mathbf{R}_r^H$, $\mathbf{R}_\theta^H$, and $\mathbf{R}_\phi^H$ have the same dimensions of $N_R \times 2M$ for EM scattering from a metal sphere and $N_R \times 4M$ for EM scattering from

a dielectric sphere. Here, N_R is the total number of receivers. These radiation matrices can be directly assembled using (9) and (14). For example, when the scatterer is a dielectric sphere, the rth row of $\mathbf{R}_r^E$ has $4M$ elements and is constructed as follows:

$$\mathbf{R}_{r,r}^E = R^2 \big[\mathbf{0} \quad \mathbf{R}_{\mathcal{L},r,1} \cdots \mathbf{R}_{\mathcal{L},r,l} \cdots \mathbf{R}_{\mathcal{L},r,L} \quad \mathbf{R}_{\mathcal{K},r,1} \cdots \mathbf{R}_{\mathcal{K},r,l} \cdots \mathbf{R}_{\mathcal{K},r,L} \quad \mathbf{0}\big] \tag{26}$$

where the second subscript r of $\mathbf{R}_{r,r}^E$, $\mathbf{R}_{\mathcal{L},r,l}$, and $\mathbf{R}_{\mathcal{K},r,l}$ denote the rth receiver, and the submatrix $\mathbf{0}$ is a row vector having M elements. $\mathbf{R}_{\mathcal{L},r,l}$ and $\mathbf{R}_{\mathcal{K},r,l}$ are evaluated using $\mathbf{l}_l^m$ in (A1a)

$$\mathbf{R}_{\mathcal{L},r,l} = \frac{-j\omega\mu\mu_0}{\eta_0} u_{l,1}^3 \cdot \left[Y_l^{-l}(\theta_r,\phi_r) \cdots Y_l^m(\theta_r,\phi_r) \cdots Y_l^l(\theta_r,\phi_r)\right] \tag{27a}$$

$$\mathbf{R}_{\mathcal{K},r,l} = v_{l,1}^2 \left[Y_l^{-l}(\theta_r,\phi_r) \cdots Y_l^m(\theta_r,\phi_r) \cdots Y_l^l(\theta_r,\phi_r)\right] \tag{27b}$$

in which $u_{l,1}^3$ and $v_{l,1}^2$ take their values at the rth receiver's radial coordinate R_r and the expressions are given in (14). Other radiation matrices can be assembled in a similar way and will not be discussed here. Finally, for the convenience of comparisons, the scattered fields obtained using (25) are converted into the values in the rectangular coordinate.

III. Numerical Results

In this section, we first present two numerical examples to verify the computation accuracy and implementation efficiency of SIM for EM scattering from a metal sphere and a dielectric sphere, respectively. The centers of both the spheres are located at the origin. The solved surface currents and scattered fields by SIM and MoM are checked against the simulation results by the commercial software Feko, which can be treated as benchmarks as long as the mesh grids are small enough. Then, the expected exponential convergence accuracy of the proposed SIM for EM scattering from a 3-D object is validated. Finally, a series of numerical experiments are performed to find the quantitative relationship between the required number of VSH modes to represent the scattered fields with different errors and the distance from the transmitter to the scatterer. In all the tests, the excitation sources are infinitesimal electric dipoles. The receiver arrays surround the sphere, are placed on its top, or are placed on the $\hat{x}$-axis. The operating frequency is 300 MHz. All the simulations and numerical computations are performed on a workstation with a 48-core Intel Xeon 6248R 3.0 G CPU and 1024 GB of memory.

A. SIM Results For EM Scattering From a Metal Sphere

As shown in Fig. 2, a metal sphere with the radius of 1.5 m and its center located at the origin is illuminated by EM waves radiated from an infinitesimal electric dipole, which is located at $(-1, 0.5, 2.4)$ m and has the polarization of $(1, 1, 1)$. Totally, there are 64 receivers surrounding the sphere and they are divided into two groups. The first 32 receivers are uniformly placed on a circular circumference located in the $\theta = 2\pi/5$ horizontal plane. The spherical coordinate of the 1st receiver is $(2.1, 2\pi/5, \pi/6)$ and the increment interval is $(0.0, 0.0, \pi/16)$.

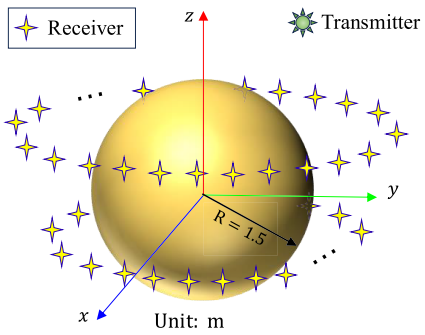

Fig. 2. Metal sphere with its center located at the origin is illuminated by EM waves excited by a 3-D infinitesimal electric dipole transmitter.

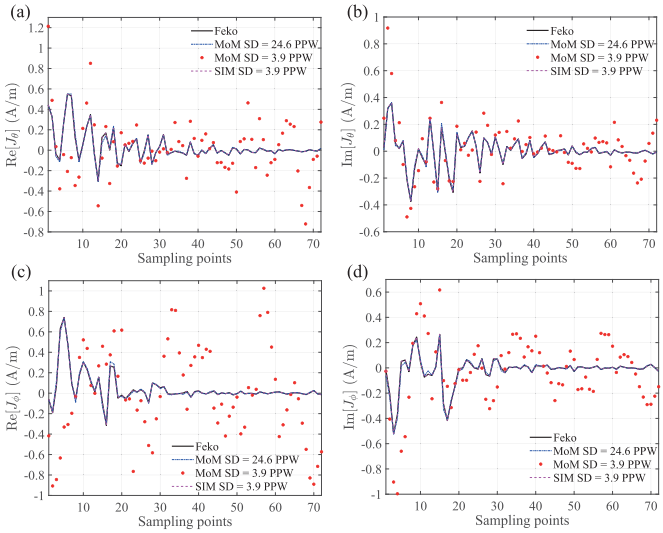

Fig. 3. Comparisons of the equivalent surface electric currents computed by Feko, MoM, and SIM when the spatial SD takes different values. (a) Real part of J_θ. (b) Imaginary part of J_θ. (c) Real part of J_ϕ. (d) Imaginary part of J_ϕ.

Similarly, the last 32 receivers are uniformly placed on the circular circumference located in the $\theta = 2\pi/3$ horizontal plane. The spherical coordinate of the 1st receiver is $(2.0, 2\pi/3, \pi/3)$ and the increment interval is also $(0.0, 0.0, \pi/16)$.

First, let us verify the correctness of the surface equivalent electric currents solved from the discretized (11). Here, we pick 72 representative sampling points on the sphere surface. The 6×12 points distribute with the same equal interval $\pi/6$ for both the polar angles and azimuthal angles. The spherical angular coordinate of the first sampling point is $(\pi/12, \pi/12)$. The surface electric currents on these points solved by Feko, MoM, and SIM with different SD values are shown in Fig. 3. The results from Feko are simulated using very dense mesh grids and thus are used as benchmarks in our work. The MoM is based on the conventional RWG basis functions and the Galerkin method. Since this is rather trivial, we will not discuss its implementation here. As can be seen, the electric current variations on the sphere surface computed by SIM match those by Feko well even when the SD of SIM is lowered to 3.9 PPW. In contrast, the traditional MoM must increase the SD to 24.6 PPW to reach relatively good matches with

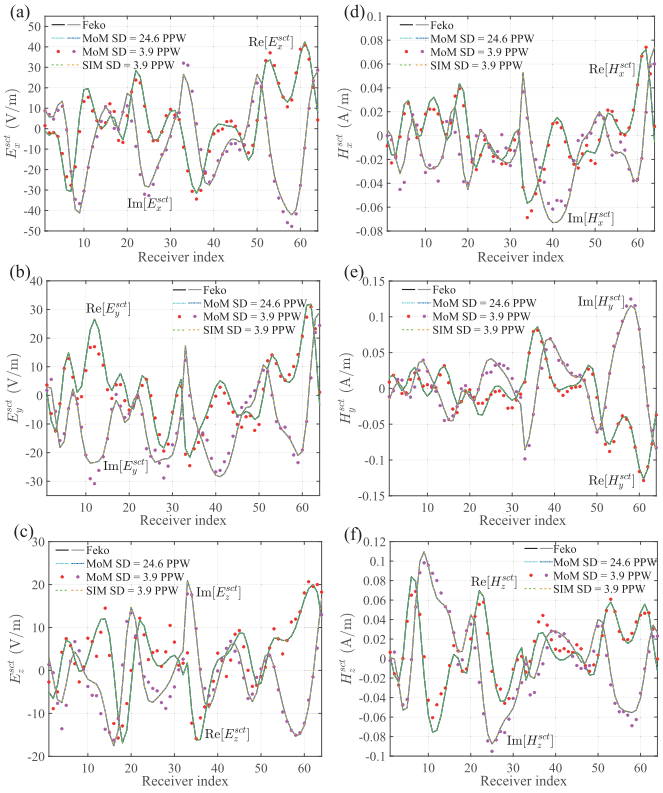

Fig. 4. Comparisons of the scattered EM fields at the receiver array computed by Feko, MoM, and SIM when the spatial SD on the sphere surface takes different values. (a) Real and imaginary parts of E_x^{sct}. (b) Real and imaginary parts of E_y^{sct}. (c) Real and imaginary parts of E_z^{sct}. (d) Real and imaginary parts of H_x^{sct}. (e) Real and imaginary parts of H_y^{sct}. (f) Real and imaginary parts of H_z^{sct}.

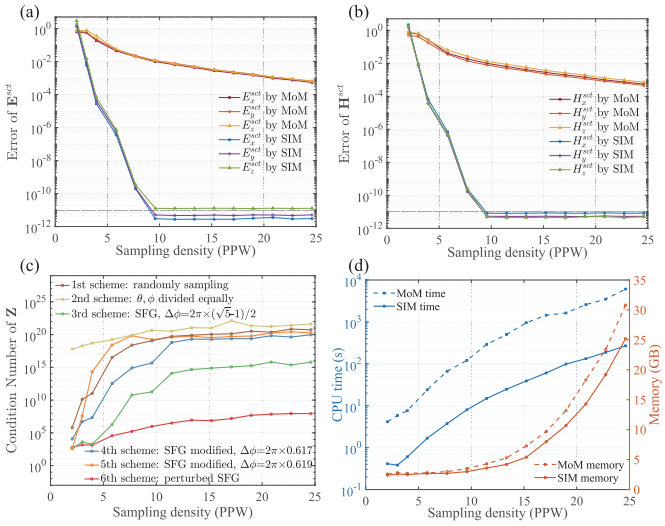

Fig. 5. Comparisons of the computation errors of scattered fields, the condition numbers of the system matrices, CPU time, and memory cost of MoM and SIM for different spatial sampling densities. (a) Errors of scattered electric fields computed by MoM and SIM. (b) Errors of scattered magnetic fields computed by MoM and SIM. (c) Condition numbers of the system matrices $\mathbf{Z}$ for six different discretization schemes in SIM. (d) CPU time and memory consumed by MoM and SIM.

the Feko results. Precise calculations show that the relative errors of J_θ for MoM with SD = 24.6 PPW, MoM with SD = 3.9 PPW, and SIM with SD = 3.9 PPW compared with Feko results are 8.3%, 161%, and 1.1%, respectively. Similarly, the relative errors of J_ϕ for the aforementioned three situations are 9.6%, 275%, and 0.8%, respectively. These error data indicate that SIM only needs around 4-PPW SD to achieve reliable computation accuracy. However, MoM needs to increase the SD to near 25 PPW to maintain the computation accuracy.

Then, let us verify the computation accuracy of scattered fields at the receiver array. We also compare the EM field values for MoM with SD = 24.6 PPW, MoM with SD = 3.9 PPW, and SIM with SD = 3.9 PPW. Fig. 4 shows the corresponding results. The relative errors of E_x^{sct} for the three situations are 0.044%, 18.4%, and 0.011%, respectively. The relative errors of E_y^{sct} are 0.052%, 21.7%, and 0.013%, respectively. The relative errors of E_z^{sct} are 0.053%, 34.7%, and 0.014%, respectively. The relative errors of H_x^{sct} are 0.047%, 26.4%, and 0.012%, respectively. The relative errors of H_y^{sct} are 0.038%, 17.6%, and 0.009%, respectively. The relative errors of H_z^{sct} are 0.058%, 24.1%, and 0.015%, respectively. It can be seen that the scattered fields at the receiver array computed by SIM can achieve the order of one ten-thousandth when the SD is lowered to 3.9 PPW. However, the SD of MoM must be increased to 24.6 PPW to reach the same error level. In addition, SIM only takes 0.6 s and consumes 2.5 GB of memory to compute the scattered fields when SD = 3.9 PPW. In contrast, when SD = 24.6 PPW, MoM takes 6066 s and consumes 30.8 GB of memory. Clearly, SIM outperforms MoM for computation efficiency when they approximately have the same computation accuracy.

Finally, let us check the exponential convergence accuracy of SIM when the spatial SD on the sphere surface gradually increases. Because the results shown in Fig. 4 confirm the reliability of the computation by SIM, we use the scattered fields by SIM when SD = 30 PPW as the criteria to compute the relative errors. Fig. 5(a) and (b) show the variations in relative errors of the scattered fields at the receiver array when SD increases from 2.0 PPW to 24.6 PPW. For SIM, when SD is less than 10.0 PPW, the error decreases exponentially. However, when SD is larger than 10.0 PPW, the error almost remains unchanged with the order of 10^{-11}. This means SD = 10.0 PPW is saturated for SIM applied to EM scattering from a metal sphere with a radius of 1.5 m. Compared with SIM, the errors of MoM decay rather slow as SD increases. Even when we increase its value to near 25 PPW, the relative errors of the scattered fields are still larger than 0.01%. Obviously, MoM can never reach the same high accuracy as SIM since it is a spatial-domain method. The solutions by MoM are obtained from the weak-form equations, and thus they only match the true values at the RWG triangle edges. Fig. 5(c) shows the variations in the condition numbers of the SIM system matrix $\mathbf{Z}$ for six different discretization schemes with the increase in the SD. We can see that sampling the field values on the sphere surface according to the azimuthal increment interval based on the golden ratio number $(\sqrt{5}-1)/2$ is critical. A small deviation will lead to a dramatic increase in the condition number. On the other hand, the condition number also grows with the increase in the SD since more

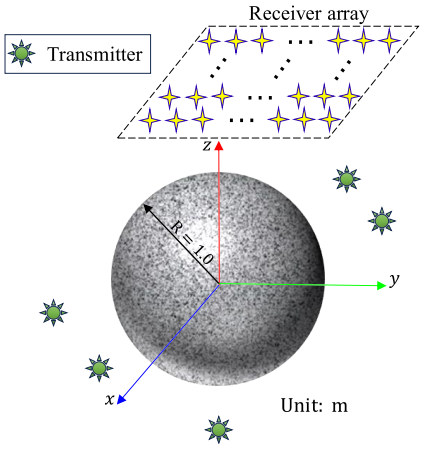

Fig. 6. Dielectric sphere with its center located at the origin is illuminated by EM waves excited by five 3-D infinitesimal electric dipole transmitters.

sampling points on the sphere surface mean higher possibility of mutual correlation of the rows or columns of the system matrix $\mathbf{Z}$. Fortunately, the small perturbation added to the SFG constructed based on the golden ratio number can significantly reduce the condition number of $\mathbf{Z}$, and thus the sixth discretization scheme is adopted in the whole work to implement the SIM. Fig. 5(d) shows the comparisons of CPU time and memory cost of SIM and MoM for different sampling densities. Obviously, for the same SD, the memory cost of SIM and MoM has no big discrepancy. The reason is that the system matrices of SIM and MoM have similar sizes in this situation. However, because MoM needs to deal with the singularity and implement the Gaussian integrals for all the mesh grids, its CPU time is much higher than that of SIM.

B. SIM Results For EM Scattering From a Dielectric Sphere

In this case, we use SIM based on the PMCHWT equations to solve EM scattering from a dielectric sphere. The model is shown in Fig. 6. The sphere has the relative permittivity of $\varepsilon_r = 2.0$, the conductivity $\sigma = 0.2$ mS/m, and the radius of 1.0 m. Its center is also located at the origin. Five electric dipole transmitters simultaneously radiate EM waves. Their rectangular coordinates are $(1.5, 0, 0.5)$ m, $(0, 1.7, 0.1)$ m, $(-1.8, 0, -0.3)$ m, $(0, -1.6, -0.8)$ m, and $(0, 0, -1.5)$ m, respectively, and their polarization is $(0.5, 2, 1)$, $(1, 0, 1)$, $(3, 1, 0.5)$, $(0, 0, 1)$, and $(1, 1, 1)$, respectively. The 8×8 receiver array is located at the $z = 1.5$ m xy-plane. The increment interval between two adjacent receivers is 0.4 m in both the $\hat{x}$- and $\hat{y}$-directions. The coordinate of the first receiver is $(x_r, y_r, z_r) = (-1.4, -1.4, 1.5)$ m.

Now, let us verify the correctness of both the electric and magnetic currents on the dielectric sphere surface solved by SIM and MoM. We also adopt the 6×12 sampling strategy similar to that used in Section III-A for the metal sphere. The angular increment interval between two adjacent points in both the $\hat{\theta}$- and $\hat{\phi}$-directions is also $\pi/6$. The spherical angular coordinate of the first sampling point is also $(\pi/12, \pi/12)$. Fig. 7 shows the comparisons of the surface electric and magnetic currents at 72 sampling points computed by

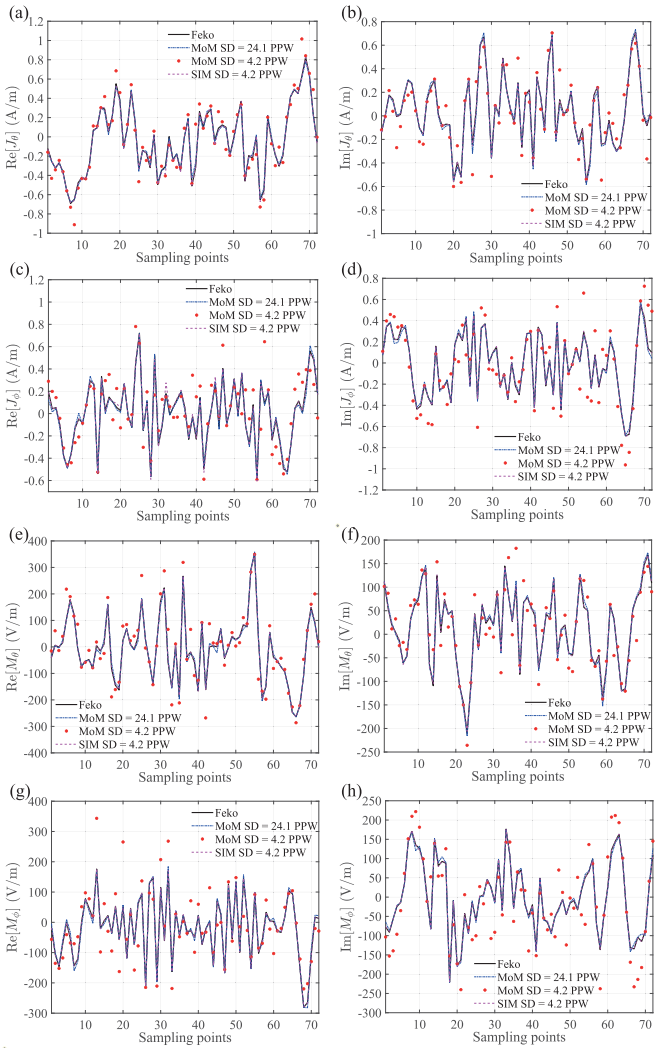

Fig. 7. Comparisons of the equivalent surface electric and magnetic currents computed by Feko, MoM, and SIM when the spatial SD takes different values. (a) Real part of J_θ. (b) Imaginary part of J_θ. (c) Real part of J_ϕ. (d) Imaginary part of J_ϕ. (e) Real part of M_θ. (f) Imaginary part of M_θ. (g) Real part of M_ϕ. (h) Imaginary part of M_ϕ.

Feko, MoM, and SIM. It is obvious that SIM based on the PWCHWT equations for EM scattering from a dielectric sphere can still reach the reliable results when the SD is as low as 4.2 PPW. However, MoM must increase the SD to six times larger to reach the same good matches with the Feko simulation results. Precise calculations show that the relative errors of J_θ for MoM with SD = 24.1 PPW, MoM with SD = 4.2 PPW, and SIM with SD = 4.2 PPW compared with Feko results are 7.1%, 36.5%, and 3.7%, respectively. The relative errors of J_ϕ are 8.0%, 64.1%, and 5.4%, respectively. The relative errors of M_θ are 7.2%, 39.7%, and 1.7%, respectively. The relative errors of M_ϕ are 7.6%, 62.2%, and 1.7%, respectively. By comparing these error data with those for the metal sphere scattering discussed in Section III-A, we can see that SIM based on the PMCHWT equations still can achieve reliable computation results for EM scattering from a dielectric sphere when the SD is low. Unfortunately, the computation of MoM is not reliable if the SD is lowered

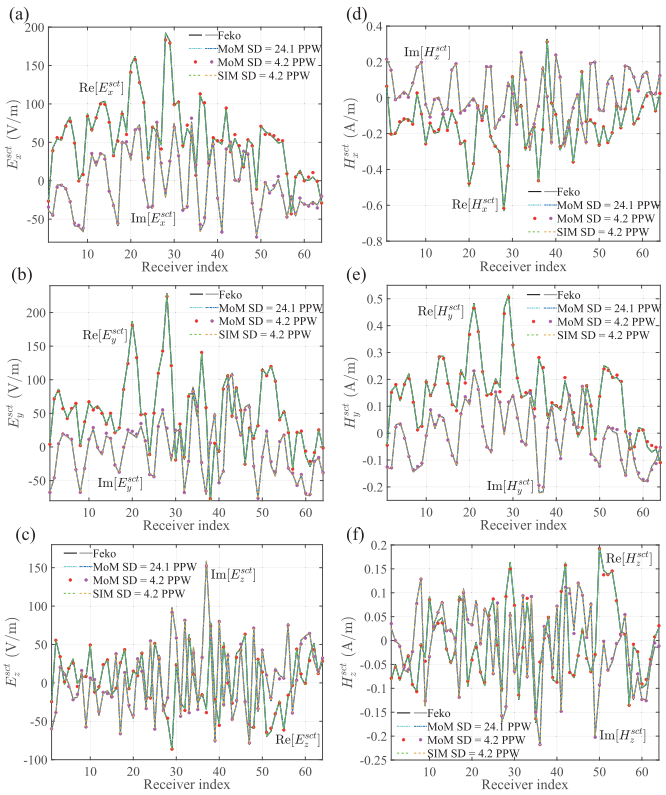

Fig. 8. Comparisons of the scattered EM fields at the receiver array computed by Feko, MoM, and SIM when the spatial SD on the sphere surface takes different values. (a) Real and imaginary parts of E_x^{sct}. (b) Real and imaginary parts of E_y^{sct}. (c) Real and imaginary parts of E_z^{sct}. (d) Real and imaginary parts of H_x^{sct}. (e) Real and imaginary parts of H_y^{sct}. (f) Real and imaginary parts of H_z^{sct}.

to near 4.0 PPW. This is further confirmed by the computed scattered fields at the receiver array which are shown in Fig. 8. The relative errors of the scattered fields are in the order of one thousandth, one percent, and one ten-thousandth for MoM with SD = 24.1 PPW, MoM with SD = 4.2 PPW, and SIM with SD = 4.2 PPW, respectively, compared with the Feko results. In addition, for this dielectric sphere EM scattering, MoM takes 39 235 s and consumes 128.6 GB of memory for SD = 24.1 PPW. However, the SIM for SD = 4.2 PPW only takes 0.76 s and consumes 2.7 GB of memory to achieve the same computation accuracy.

Fig. 9(a) and (b) shows the variations in relative errors of the scattered fields at the 64 receivers for different SD values. We can see that SIM based on the PMCHWT equations still has the exponential convergence accuracy for EM scattering from a dielectric sphere. However, compared with the error variations shown in Fig. 5(a) and (b) for metal sphere scattering, the errors of both SIM and MoM decay slower for dielectric sphere scattering. The possible reason for such a difference is that both the electric and magnetic currents are induced on the surface of a dielectric sphere. This actually enhances the complexity of the scattering problem, and thus higher sampling densities are required to obtain the accurate solutions. Fig. 9(c) shows the variations in the condition numbers of the SIM system matrix $\mathbf{Z}$ with the increase in the SD. We can see that the 6th scheme of the perturbed SFG still has the lowest

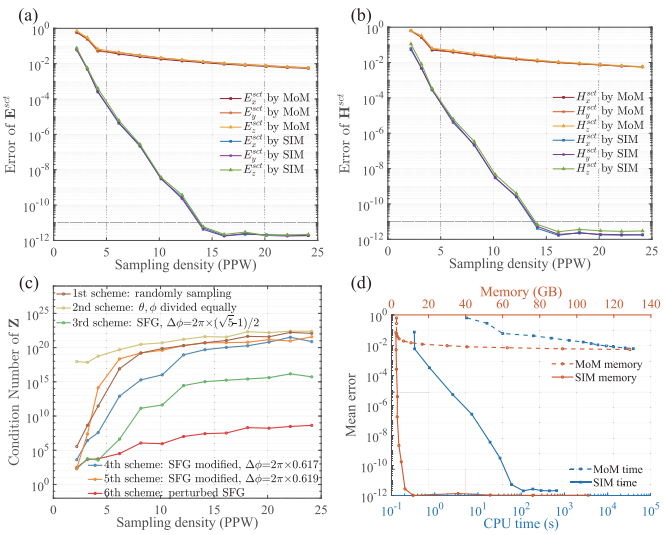

Fig. 9. Comparisons of the computation errors of scattered fields, the condition numbers of the system matrices, CPU time, and memory cost of MoM and SIM for different spatial sampling densities. (a) Errors of scattered electric fields computed by MoM and SIM. (b) Errors of scattered magnetic fields computed by MoM and SIM. (c) Condition numbers of the system matrices $\mathbf{Z}$ for six different discretization schemes in SIM. (d) Mean errors of the scattered fields versus CPU time and memory cost for MoM and SIM.

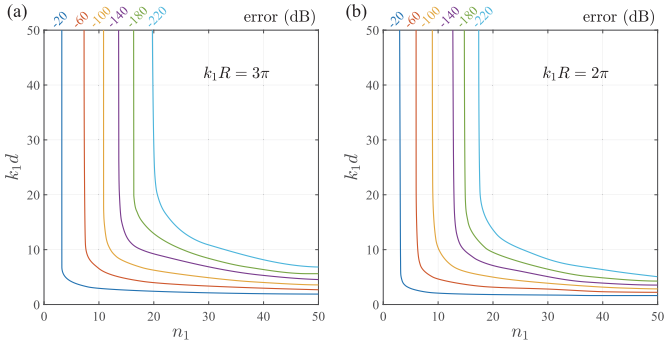

Fig. 10. Quantitative relationship between six typical computation errors of the scattered fields and k_1d and n_1. (a) Metal sphere with $k_1R = 3\pi$. (b) Dielectric sphere with $k_1R = 2\pi$.

condition number value for the SIM based on the PMCHWT equations. Fig. 9(d) shows the CPU time and the memory cost versus the mean errors of the scattered fields when SD increases from 2.0 to 24.1 PPW. Obviously, the error of SIM is much lower than that of MoM for the same CPU time or memory cost. In other words, MoM will consume much more computational resources than SIM if we try to use both of them to reach the same accuracy.

C. Required Number of VSH Modes to Accurately Represent Scattered Fields

By referring to [34], we also try to quantify the required number of VSH modes or the truncated threshold L in (7) to represent the scattered fields with certain errors subject to near- or far-field excitation of the transmitter. To find the dependence of errors on L and the transmitter distance from the scatterer, we perform a series of numerical experiments for both the metal sphere and the dielectric sphere. The receiver

is fixed in the $\hat{x}$-axis and $5\lambda_1$ from the sphere surface. Here, λ_1 is the wavelength of the background medium. A series of transmitters are placed on the $\hat{z}$-axis and have the polarization of (1, 1, 1). Their distances d to the sphere surface vary between 0 and $50/2\pi$ m. Based on [34, eq. (2.31)], we assume the required truncated threshold L can be estimated by the following equation:

$$L = \lfloor k_1 R \rfloor + n_1 \tag{28}$$

in which k_1 is the wavenumber of the background medium, n_1 is a compensation integer, and $\lfloor \cdot \rfloor$ denotes the largest integer less than or equal to the given parameter. We now choose six fixed errors, −20, −60, −100, −140, −180, and −220 dB. They are the average errors for six components of the scattered fields and computed with respect to the results for SD = 30 PPW. The quantitative relationship curves between $k_1 d$ and n_1 for EM scattering from both the metal sphere and the dielectric sphere are shown in Fig. 10. Several observations are made here. First, the curves for our EM scattering problems have the similar variation trends as those shown in [34, Fig. 2.6] which are evaluated for antenna radiation problems. When $d > 5\lambda_1$, the saturation error is almost independent of d. In contrast, when $d < \lambda_1$, the computation error strongly depends on d. In this situation, larger values of n_1 are necessary to guarantee the accuracy of the computed scattered fields. Second, reducing the sphere radius results in a consistent leftward shift of the whole family of curves, which indicates the decrease of n_1 to maintain the same computation error. It is found that n_1 for the saturation error is approximately scaled by 0.8819 when $k_1 R$ is decreased from 3π to 2π in our EM scattering problems, which is roughly consistent with the predicted ratio of $\sqrt[3]{2/3}$ from the scaling formula $\sqrt[3]{k_1 R}$ in analysis of [34, Fig. 2.6] for antenna radiation problems. Third, for the far-field illumination, i.e., when d is larger than $5\lambda_1$, to maintain the computation error in the order of −80 dB, we suggest $n_1 = 9$ for the metal sphere with $k_1 R = 3\pi$ and $n_1 = 8$ for the dielectric sphere with $k_1 R = 2\pi$. These values of n_1 are slightly less that provided in [34]. Of course, these empirical choices are highly dependent on the scatterer parameters. Unfortunately, there is no suggested n_1 value for the near-field illumination since it highly depends on the distance d. Fourth, the required number of VSH modes to represent the scattered fields is $L^2 + 2L$ in our problem. In contrast, it is two times in the antenna radiation problems with two probe orientations based on [34, eq. (4.136)]. Correspondingly, the numbers of sampling points in our problem are $2L^2 + 4L$ for the EFIE and $4L^2 + 8L$ for the PMCHWT equations. In the antenna measurements, the numbers of sampling points are $2(2L + 1)(L + 1)$ and $(4/\pi)(2L + 1)(L + 1)$ based on [34, eqs. (4.137) and (4.138)].

IV. Summary, Conclusion, and Future Work

In this work, we developed the SIM for EM scattering from a 3-D sphere that is filled with metal or homogeneous dielectric material. Both the equivalent surface currents and DGFs are expanded using VSH series and thus the original convolutional integral in the SIE is transformed into the multiplication of VSH coefficients of the currents and DGFs. The infinite number of terms of the DGF expansion caused by its singularity is automatically truncated by the finite terms of the surface current expansion. Therefore, both the EFIE and PMCHWT equations for EM scattering from a 3-D sphere are solved in the spectral domain with a limited number of VSH coefficients but without losing the high accuracy.

Two numerical examples are first used to validate the superiority of the proposed SIM to the traditional MoM. For EM scattering from a smooth 3-D metal sphere, SIM can achieve reliable computation accuracy of the scattered fields, i.e., the error is in the order of one ten-thousandth, when the spatial SD reaches 4.0 PPW. In contrast, the traditional MoM needs nearly 25.0 PPW to reach the same order of computation accuracy. When the scatterer is a dielectric sphere, MoM can only lower the computation error of the scattered fields to the order of one thousandth if we increase the SD to 25.0 PPW. SIM is able to maintain computation accuracy with low computational cost for EM scattering from both metal and dielectric spheres. Then, a series of numerical experiments are performed to investigate the required number of VSH modes to accurately represent the scattered fields. It is found that the number can be approximated by the integer part of the product of the wavenumber and the sphere radius, plus a compensation number. This number is independent of the separation distance between the transmitter and the scatterer under far-field conditions but exhibits a strong dependence on this distance under near-field conditions. Finally, it is worth mentioning that although the excitation sources are dipoles in this work, the proposed SIM can be directly used to compute the EM scattering from smooth spheres illuminated by plane waves. Numerical simulations show that the radar cross sections (RCSs) computed by SIM checked against the Mie series solutions have the errors at the level of machine precision.

The future work will be focused in five aspects.

1) Develop SIM for EM scattering from a 3-D object with a general smooth shape, e.g., an ellipsoid. Because we only exercise SIM on a canonical sphere in this work, the original integral $\int_S \overline{\overline{\mathbf{G}}} \cdot \{\} dS' = \int_0^{2\pi} \int_0^{\pi} \overline{\overline{\mathbf{G}}} \cdot \{\} r'^2 \sin\theta' \phi d\theta' d\phi'$ in SIE can be transformed into $R^2 \int_0^{2\pi} \int_0^{\pi} \overline{\overline{\mathbf{G}}} \cdot \{\} \sin\theta' \phi d\theta' d\phi'$ since r' is constant with the variation of the solid angle. Unfortunately, this is incorrect for noncanonical smooth objects. Therefore, it is necessary to expand $\overline{\overline{\mathbf{G}}}(r', \theta', \phi') r'^2(\theta', \phi')$ instead of $\overline{\overline{\mathbf{G}}}(R, \theta', \phi')$ using VSH series when implementing the SIM. Because $\overline{\overline{\mathbf{G}}}$ has singularity, it must be removed before performing the numerical integration to compute the VSH coefficients of $\overline{\overline{\mathbf{G}}} r'^2$. Similar problems have been discussed in detail in [23] and [25] for EM scattering from 2-D cylinders.
2) Develop SIM for EM scattering from smooth 3-D objects with multiple layers, e.g., radome. The mutual coupling of EM waves between adjacent boundaries also must be formulated using SIM. Similar 2-D results have been shown in our previous works [24], [25]. Note that even for multilayered spheres, as long as they are nonconcentric, we must expand $\overline{\overline{\mathbf{G}}} r'^2$ instead of only $\overline{\overline{\mathbf{G}}}$ using VSH series.

3) Develop SIM for smooth 3-D objects filled with homogeneous anisotropic material. These kinds of designs are always used to manipulate the EM wave propagation, e.g., classic spherical cloaking [35]. Since the DGF has no analytical expansion of the VSH series for anisotropic dielectric parameters, numerical integration with the singularity extraction is also necessary to compute the spectral coefficients. In our previous works, the SIM for EM scattering from 2-D cylinders filled with biaxially anisotropic materials has been validated [25], [27].
4) Investigate the dependence of the required number of VSH modes on the separation distance between the spherical scatterer and the excitation source with an arbitrary current distribution. This is the extension of the contents presented in Section III-C in which the source is an infinitesimal dipole. The previous work [36] has provided the reference method for the spherical harmonic expansion of the EM waves radiated by an arbitrary source.
5) Hybridize SIM with other DE-based methods such as SEM to compute EM scattering from 3-D inhomogeneous objects. Because SIM can maintain the computation accuracy with low SD, it outperforms the traditional surface MoM to truncate the computation domain of SEM in the implementation efficiency. Similar strategies have been verified in [26] and [27] for 2-D EM scattering.

APPENDIX

The VSH are complex-valued basis functions used to expand 3-D vector fields in solid angular space. Based on [28] and [29, eqs. (7)–(9)], they can be constructed as follows:

$$\mathbf{l}_l^m(\theta,\phi) = Y_l^m(\theta,\phi)\,\hat{r} \tag{A1a}$$

$$\mathbf{m}_l^m(\theta,\phi) = \frac{1}{\sqrt{l(l+1)}}\left[\frac{1}{\sin\theta}\frac{\partial Y_l^m(\theta,\phi)}{\partial\phi}\hat{\theta} - \frac{\partial Y_l^m(\theta,\phi)}{\partial\theta}\hat{\phi}\right] \tag{A1b}$$

$$\mathbf{n}_l^m(\theta,\phi) = \frac{1}{\sqrt{l(l+1)}}\left[\frac{\partial Y_l^m(\theta,\phi)}{\partial\theta}\hat{\theta} + \frac{1}{\sin\theta}\frac{\partial Y_l^m(\theta,\phi)}{\partial\phi}\hat{\phi}\right] \tag{A1c}$$

where Y_l^m is the SSH and it is constructed as follows:

$$Y_l^m(\theta,\phi) = C_l^m P_l^m(\cos\theta)\,e^{-jm\phi} \tag{A2}$$

in which the coefficient C_l^m is written as follows:

$$C_l^m = \sqrt{\frac{2l+1}{4\pi}\frac{(l-m)!}{(l+m)!}} \tag{A3}$$

where ! is the factorial operation. Note P_l^m in (A2) is the lth-order associated Legendre polynomial which represents the harmonic in the polar $\hat{\theta}$-direction and $e^{-jm\phi}$ is the mth-order Fourier harmonic in the azimuthal $\hat{\phi}$-direction. Note the orthogonality of the VSH has been proven in [28] and [37] and its completeness has been proven in [38]. They will not be discussed here anymore. Using the VSH in (A1), the electric-type DGF $\overline{\overline{\mathbf{G}}}_e$ and the magnetic-type DGF $\overline{\overline{\mathbf{G}}}_m$ can be, respectively, expanded as [8], [39]

$$\begin{aligned}\overline{\overline{\mathbf{G}}}_e(r,\theta,\phi,r',\theta',\phi') = -jk\sum_{l=1}^{\infty}\sum_{m=-l}^{l}\\ C_1\mathbf{m}_l^m(\theta,\phi)\,\mathbf{m}_l^{m*}(\theta',\phi') + \frac{1}{k^2rr'}\left[C_2\mathbf{n}_l^m(\theta,\phi)\,\mathbf{n}_l^{m*}(\theta',\phi')\right.\\ \left.+\,l(l+1)\,C_1\mathbf{l}_l^m(\theta,\phi)\,\mathbf{l}_l^{m*}(\theta',\phi')\right] + \frac{\sqrt{l(l+1)}}{k^2rr'}\\ \times\left\{\left[\frac{C_3+C_4}{2} + \frac{C_3-C_4}{2}\cdot\mathrm{sgn}(r'-r)\right]\mathbf{n}_l^m(\theta,\phi)\,\mathbf{l}_l^{m*}(\theta',\phi')\right.\\ \left.+\left[\frac{C_3+C_4}{2} + \frac{C_3-C_4}{2}\cdot\mathrm{sgn}(r-r')\right]\mathbf{l}_l^m(\theta,\phi)\,\mathbf{n}_l^{m*}(\theta',\phi')\right\}\end{aligned} \tag{A4a}$$

$$\begin{aligned}\overline{\overline{\mathbf{G}}}_m(r,\theta,\phi,r',\theta',\phi') = -jk\sum_{l=1}^{\infty}\sum_{m=-l}^{l}\\ \sqrt{l(l+1)}C_1\left[\frac{1}{r}\mathbf{l}_l^m(\theta,\phi)\,\mathbf{m}_l^{m*}(\theta',\phi') + \frac{1}{r'}\mathbf{m}_l^m(\theta,\phi)\,\mathbf{l}_l^{m*}(\theta',\phi')\right]\\ +\frac{1}{r'}\left[\frac{C_3+C_4}{2} + \frac{C_3-C_4}{2}\cdot\mathrm{sgn}(r-r')\right]\mathbf{m}_l^m(\theta,\phi)\,\mathbf{n}_l^{m*}(\theta',\phi')\\ +\frac{1}{r}\left[\frac{C_3+C_4}{2} + \frac{C_3-C_4}{2}\cdot\mathrm{sgn}(r'-r)\right]\mathbf{n}_l^m(\theta,\phi)\,\mathbf{m}_l^{m*}(\theta',\phi')\end{aligned} \tag{A4b}$$

where sgn is the Signum function and the coefficients C_1, C_2, C_3, and C_4 are not constants. Instead, they change with the radial variables r and r' and can be constructed as follows:

$$\begin{cases} C_1(r,r') = h_l^{(2)}(kr_>)\,j_l(kr_<)\\ C_2(r,r') = \dfrac{\partial\left[r_>h_l^{(2)}(kr_>)\right]}{\partial r_>}\dfrac{\partial\left[r_<j_l(kr_<)\right]}{\partial r_<}\\ C_3(r,r') = h_l^{(2)}(kr_>)\dfrac{\partial\left[r_<j_l(kr_<)\right]}{\partial r_<}\\ C_4(r,r') = j_l(kr_<)\dfrac{\partial\left[r_>h_l^{(2)}(kr_>)\right]}{\partial r_>}\end{cases} \tag{A5}$$

in which $r_>$ takes the larger value of r and r' while $r_<$ takes the smaller value of r and r'. j_l is the spherical Bessel function, $h_l^{(2)}$ is the spherical Hankel function of the second kind, and l is their orders. They are related to the regular cylindrical Bessel and Hankel functions by $j_l(x) = \sqrt{\pi/2x}J_{n+1/2}(x)$ and $h_l^{(2)}(x) = \sqrt{\pi/2x}H_{n+1/2}^{(2)}(x)$. One should note that (A4a) and (A4b) still hold true when $r = r'$ although this situation is rarely discussed in literature due to the singularities of $\overline{\overline{\mathbf{G}}}_e$ and $\overline{\overline{\mathbf{G}}}_m$ in the solid angle space. First, the coefficients C_1 and C_2 are continuous when r and r' approach each other. Therefore, their values evaluated at $r = r'$ can be directly used in the coefficients of $\mathbf{m}_l^m\mathbf{m}_l^{m*}$, $\mathbf{n}_l^m\mathbf{n}_l^{m*}$, or $\mathbf{l}_l^m\mathbf{l}_l^{m*}$ of $\overline{\overline{\mathbf{G}}}_e$ and the coefficients of $\mathbf{l}_l^m\mathbf{m}_l^{m*}$ or $\mathbf{m}_l^m\mathbf{l}_l^{m*}$ of $\overline{\overline{\mathbf{G}}}_m$ when $r = r'$ since it is the limit of $r \to r'$ and $r' \to r$. Second, although the coefficients of $\mathbf{n}_l^m\mathbf{l}_l^{m*}$ and $\mathbf{l}_l^m\mathbf{n}_l^{m*}$ of $\overline{\overline{\mathbf{G}}}_e$ and the coefficients $\mathbf{m}_l^m\mathbf{n}_l^{m*}$ and $\mathbf{n}_l^m\mathbf{m}_l^{m*}$ of $\overline{\overline{\mathbf{G}}}_m$ are discontinuous when r and r' approach each other, we can judiciously let their values at $r = r'$ take the average values of the corresponding coefficients evaluated using C_3 and C_4

individually. This is directly manifested by the zero value of the Signum function for $r = r'$ in (A4a) and (A4b). Such a strategy of using average values is reasonable since the value of a periodic function at its nonsmooth point is equal to the average value of its left limit and the right limit at that point. On the other hand, numerical experiments show that evaluating the coefficients of $\mathbf{n}_l^m \mathbf{l}_l^{m*}$ and $\mathbf{l}_l^m \mathbf{n}_l^{m*}$ of $\overline{\overline{\mathbf{G}}}_e$ and the coefficients of $\mathbf{m}_l^m \mathbf{n}_l^{m*}$ and $\mathbf{n}_l^m \mathbf{m}_l^{m*}$ of $\overline{\overline{\mathbf{G}}}_m$ at $r = r'$ using a huge number of Gaussian integral points can exactly come to the average value of the analytical coefficients of these dyadics for $r > r'$ and $r < r'$.

REFERENCES

[1] L. Tsang, J. A. Kong, and K.-H. Ding, *Scattering of Electromagnetic Waves: Theories and Applications*. Hoboken, NJ, USA: Wiley, 2000.

[2] W. Li et al., "Intelligent metasurface system for automatic tracking of moving targets and wireless communications based on computer vision," *Nature Commun.*, vol. 14, no. 1, p. 989, Feb. 2023.

[3] J. Schofield, D. Daniels, and P. Hammerton, "A multiple migration and stacking algorithm designed for land mine detection," *IEEE Trans. Geosci. Remote Sens.*, vol. 52, no. 11, pp. 6983–6988, Nov. 2014.

[4] F. García-Rial, D. Montesano, I. Gómez, C. Callejero, F. Bazus, and J. Grajal, "Combining commercially available active and passive sensors into a millimeter-wave imager for concealed weapon detection," *IEEE Trans. Microw. Theory Techn.*, vol. 67, no. 3, pp. 1167–1183, Mar. 2019.

[5] L. Zou, L. Yi, and M. Sato, "On the use of lateral wave for the interlayer debonding detecting in an asphalt airport pavement using a multistatic GPR system," *IEEE Trans. Geosci. Remote Sens.*, vol. 58, no. 6, pp. 4215–4224, Jun. 2020.

[6] S. Yang, J. Wang, J. Zhou, T. Zhu, and H. Wang, "An efficient algorithm of both Fréchet derivative and inversion of MCIL data in a deviated well in a horizontally layered TI formation based on TLM modeling," *IEEE Trans. Geosci. Remote Sens.*, vol. 52, no. 11, pp. 6911–6923, Nov. 2014.

[7] C. A. Balanis, *Advanced Engineering Electromagnetics*. Hoboken, NJ, USA: Wiley, 2012, ch. 7.

[8] W. C. Chew, *Waves and Fields in Inhomogeneous Media*. New York, NY, USA: IEEE Press, 1995, ch. 7.

[9] L. E. Sun, "Electromagnetic modeling of inhomogeneous and anisotropic structures by volume integral equation methods," *Waves Random Complex Media*, vol. 25, no. 4, pp. 536–548, Oct. 2015.

[10] H.-W. Zhang, X.-W. Huang, and X.-Q. Sheng, "Surface integral equation solutions for electromagnetic scattering from a special class of anisotropic media," *IEEE Trans. Antennas Propag.*, vol. 70, no. 9, pp. 8204–8215, Sep. 2022.

[11] R. F. Harrington, *Field Computation By Moment Methods*. Hoboken, NJ, USA: Wiley, 1993.

[12] P. Zwamborn and P. M. van den Berg, "The three dimensional weak form of the conjugate gradient FFT method for solving scattering problems," *IEEE Trans. Microw. Theory Techn.*, vol. 40, no. 9, pp. 1757–1766, Sep. 1992.

[13] S. Rao, D. Wilton, and A. Glisson, "Electromagnetic scattering by surfaces of arbitrary shape," *IEEE Trans. Antennas Propag.*, vol. AP-30, no. 3, pp. 409–418, May 1982.

[14] D. Schaubert, D. Wilton, and A. Glisson, "A tetrahedral modeling method for electromagnetic scattering by arbitrarily shaped inhomogeneous dielectric bodies," *IEEE Trans. Antennas Propag.*, vol. AP-32, no. 1, pp. 77–85, Jan. 1984.

[15] F. Han, J. Zhuo, N. Liu, Y. Liu, H. Liu, and Q. H. Liu, "Fast solution of electromagnetic scattering for 3-D inhomogeneous anisotropic objects embedded in layered uniaxial media by the BCGS-FFT method," *IEEE Trans. Antennas Propag.*, vol. 67, no. 3, pp. 1748–1759, Mar. 2019.

[16] E. Bleszynski, M. Bleszynski, and T. Jaroszewicz, "AIM: Adaptive integral method for solving large-scale electromagnetic scattering and radiation problems," *Radio Sci.*, vol. 31, no. 5, pp. 1225–1251, Sep. 1996.

[17] J. Song, C.-C. Lu, and W. Cho Chew, "Multilevel fast multipole algorithm for electromagnetic scattering by large complex objects," *IEEE Trans. Antennas Propag.*, vol. 45, no. 10, pp. 1488–1493, Oct. 1997.

[18] W. Hergert and T. Wriedt, *The Mie Theory: Basics and Applications*. Cham, Switzerland: Springer, 2012.

[19] F. Vernì, M. Righero, and G. Vecchi, "On the use of entire-domain basis functions and fast factorizations for the design of modulated metasurface," *IEEE Trans. Antennas Propag.*, vol. 68, no. 5, pp. 3824–3833, May 2020.

[20] W.-Y. Tam and K.-M. Luk, "Resonance in spherical-circular microstrip structures," *IEEE Trans. Microw. Theory Techn.*, vol. 39, no. 4, pp. 700–704, Apr. 1991.

[21] W. Y. Tam, "Input impedance of spherical microstrip antenna," *IEE Proc.-Microw., Antennas Propag.*, vol. 142, no. 3, pp. 285–288, Jun. 1995.

[22] Z. Sipus, N. Burum, S. Skokic, and P.-S. Kildal, "Analysis of spherical arrays of microstrip antennas using moment method in spectral domain," *IEE Proc.-Microw., Antennas Propag.*, vol. 153, no. 6, pp. 533–543, 2006.

[23] F. Q. Hu, "A spectral boundary integral equation method for the 2D Helmholtz equation," *J. Comput. Phys.*, vol. 120, no. 2, pp. 340–347, Sep. 1995.

[24] Z. Guan, Y. Zhang, F. Han, C. Zhu, and Q. H. Liu, "Fast exponentially convergent solution of electromagnetic scattering from multilayer concentric magnetodielectric cylinders by the spectral integral method," *IEEE Trans. Microw. Theory Techn.*, vol. 68, no. 6, pp. 2183–2193, Jun. 2020.

[25] Z. Guan, J. Li, and F. Han, "Exponential accuracy solutions of 2-D electromagnetic scattering from multilayered nonconcentric elliptical magnetodielectric cylinders under TE illumination," *IEEE Trans. Microw. Theory Techn.*, vol. 72, no. 5, pp. 2914–2926, May 2024.

[26] Z. Guan, J. Liu, M. Zhuang, and Q. H. Liu, "A hybrid SESI method for electromagnetic scattering by objects in multiregion cylindrically layered media," *IEEE Trans. Microw. Theory Techn.*, vol. 69, no. 9, pp. 3967–3975, Sep. 2021.

[27] Z. Guan, J. Li, and F. Han, "2-D electromagnetic scattering from multiple arbitrarily anisotropic inhomogeneities embedded in multilayered biaxially anisotropic elliptical cylinders solved by the hybrid SIM/SEM," *IEEE Trans. Antennas Propag.*, vol. 72, no. 8, pp. 6849–6854, Aug. 2024.

[28] J. A. Stratton, *Electromagnetic Theory*. New York, NY, USA: McGraw-Hill, 1941, ch. 7, pp. 414–418.

[29] G. C. Kokkorakis and J. G. Fikioris, "EM field induced in inhomogeneous dielectric spheres by external sources," *IEEE*, vol. 55, no. 11, pp. 3178–3190, Nov. 2007.

[30] J. Hu and C. Sideris, "A high-order-accurate 3D surface integral equation solver for uniaxial anisotropic media," *IEEE Trans. Antennas Propag.*, vol. 71, no. 5, pp. 4262–4271, May 2023.

[31] H. Lin, J. Zhuo, M. Zhuang, Z. He, and Q. Huo Liu, "A 3-D MoM for uniaxial objects with an arbitrary optical axis embedded in uniaxial multilayers," *IEEE Trans. Microw. Theory Techn.*, vol. 72, no. 10, pp. 5768–5778, Oct. 2024.

[32] J. Liu and Q. Huo Liu, "A spectral integral method (SIM) for periodic and nonperiodic structures," *IEEE Microw. Wireless Compon. Lett.*, vol. 14, no. 3, pp. 97–99, Mar. 2004.

[33] R. Marques, C. Bouville, K. Bouatouch, and J. Blat, "Extensible spherical Fibonacci grids," *IEEE Trans. Vis. Comput. Graphics*, vol. 27, no. 4, pp. 2341–2353, Apr. 2021.

[34] J. E. Hansen, *Spherical Near-Field Antenna Measurements*. London, U.K.: The Institution of Engineering and Technology, 1989, chs. 2–4.

[35] L. Gao, T. H. Fung, K. W. Yu, and C. W. Qiu, "Electromagnetic transparency by coated spheres with radial anisotropy," *Phys. Rev. E, Stat. Phys. Plasmas Fluids Relat. Interdiscip. Top.*, vol. 78, no. 4, Oct. 2008, Art. no. 046609.

[36] B. Fuchs, S. Palud, L. Le Coq, O. Lafond, M. Himdi, and S. Rondineau, "Scattering of spherically and hemispherically stratified lenses fed by any real source," *IEEE Trans. Antennas Propag.*, vol. 56, no. 2, pp. 450–460, Feb. 2008.

[37] P. M. Morse and H. Feshbach, *Methods of Theoretical Physics*. New York, NY, USA: McGraw-Hill, 1953, pp. 1898–1900.

[38] K. Aydin and A. Hizal, "On the completeness of the spherical vector wave functions," *J. Math. Anal. Appl.*, vol. 117, no. 2, pp. 428–440, Aug. 1986.

[39] C.-T. Tai, *Dyadic Green Functions in Electromagnetic Theory*. New York, NY, USA: Institute of Electrical and Electronics Engineers, 1994, ch. 10.